analytical chemistry

pubs.acs.org/ac Article

PepDRED: De Novo Peptide Design with Strong Binding Affinity for Target Protein

Mehmoona Azmat, Behafarid Ghalandari, Jessica Jessica, Yuechen Xu, Xinle Li, Wenqiong Su, Zhang Qiang, Shuxin Deng, Tabina Azmat, Lai Jiang,* and Xianting Ding*

Cite This: *Anal. Chem.* 2023, 95, 12264−12272 Read Online

ACCESS | Metrics & More | Article Recommendations | Supporting Information

ABSTRACT: De novo design of peptides that bind specifically to functional proteins is beneficial for diagnostics and therapeutics. However, complex permutations and combinations of amino acids pose significant challenges to the rational design of peptides with desirable stability and affinity. Herein, we develop a computational-based evolution method, namely, peptidomimetics-driven recognition elements design (PepDRED), to derive hemoglobin-inspired peptidomimetics. PepDRED mimics the natural evolutionism pipeline to generate stable apovariant (AVs) structures for wild-type counterparts via automated point mutations and validates their efficiency through free binding energy analysis and per residue energy decomposition analysis. For application demonstration, we applied PepDRED to design de novo peptides to bind FhuA, a typical TonB-dependent transporter (TBDT). TBDTs are Gram-negative bacterial outer membrane proteins responsible for iron transport and vital for bacterial resistance. PepDRED generated a pool of AVs and proceeded to reach an optimized peptide, AV440, with a remarkable binding affinity of −21 kcal/mol. AV440 is ∼2.5-fold stronger than the existing FhuA inhibitor Microcin J25. Network energy analysis further unveils that incorporating methionine (M42) in the N-terminal region significantly enhances inter-residue contacts and binding affinity. PepDRED offers a prompt and efficient in silico approach to develop potent peptide candidates for target proteins.

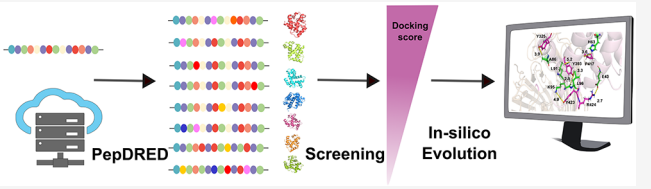

INTRODUCTION

Rapid detection of pathogenic bacteria facilitates the decrease of sporadic outbreaks, nosocomial infectious dissemination, and public health economic burden.[1] Standard methods of bacterial detection can be sensitive and specific. Yet, their processing time is lengthy and thus are frequently precluded in resource-limited settings leading to the misuse of antibiotics.[2] In turn, the implications of the rising incidence of antimicrobial resistance (AMR) are becoming an alarming global public health concern.[3] Consequently, it is a constant challenge to develop rapid early-stage bacterial biosensing technologies to reduce the risk of these emerging infectious diseases and mitigate AMR.

Bacterial biosensors are emerging tools for rapid diagnostics and detection of pathogens and their drug-resistant variants. In simplest formation, they are composed of biological recognition elements (BREs) and signal probes.[4] Identifying BREs with strong binding affinity and specificity to target biomarkers is critical for biosensor performance.[5] Currently, these limitations restrict the broad use of biosensors with real samples. This challenge requires a rapid and readily optimizable architecture and a selection of correct biological and chemical modalities to recognize the target.[6] At present, bacterial biosensors have been designed using various BREs such as enzymes, aptamers (single-strand DNA or RNA), antibodies, carbohydrates, and a mix of these motifs.[7−11] Generally, affinity-based sensors (antibodies and aptamers) are preferred over enzymatic biosensors due to their enhanced selectivity and specificity and the lack of extra reagents required.[12] However, the stability of these elements in biological media is usually lower because of the interfering components (the composition of the sample) and sample conditions (pH, viscosity), as well as nonspecific binding, which affects their activity.[8,13] Multiple alternative modalities have been probed to overcome the inherent difficulties of BREs. Peptides provide an attractive and viable approach to designing BREs.[14] Through their secondary structures, peptides have the extraordinary recognition flexibility to adapt sterically and establish many forms of noncovalent interactions with target molecules.[15] In addition, peptides are renowned for their desired selectivity due to their capacity to interact with multiple binding sites on target molecules.[16] Peptides can be widely applied as BREs in the design of early bacterial sensing.[17,18] A significant need for early detection is presented by Gram-negative bacterial (GNB) Enterobacter-

Received: March 9, 2023
Accepted: July 23, 2023
Published: August 8, 2023

https://doi.org/10.1021/acs.analchem.3c01057
Anal. Chem. 2023, 95, 12264−12272

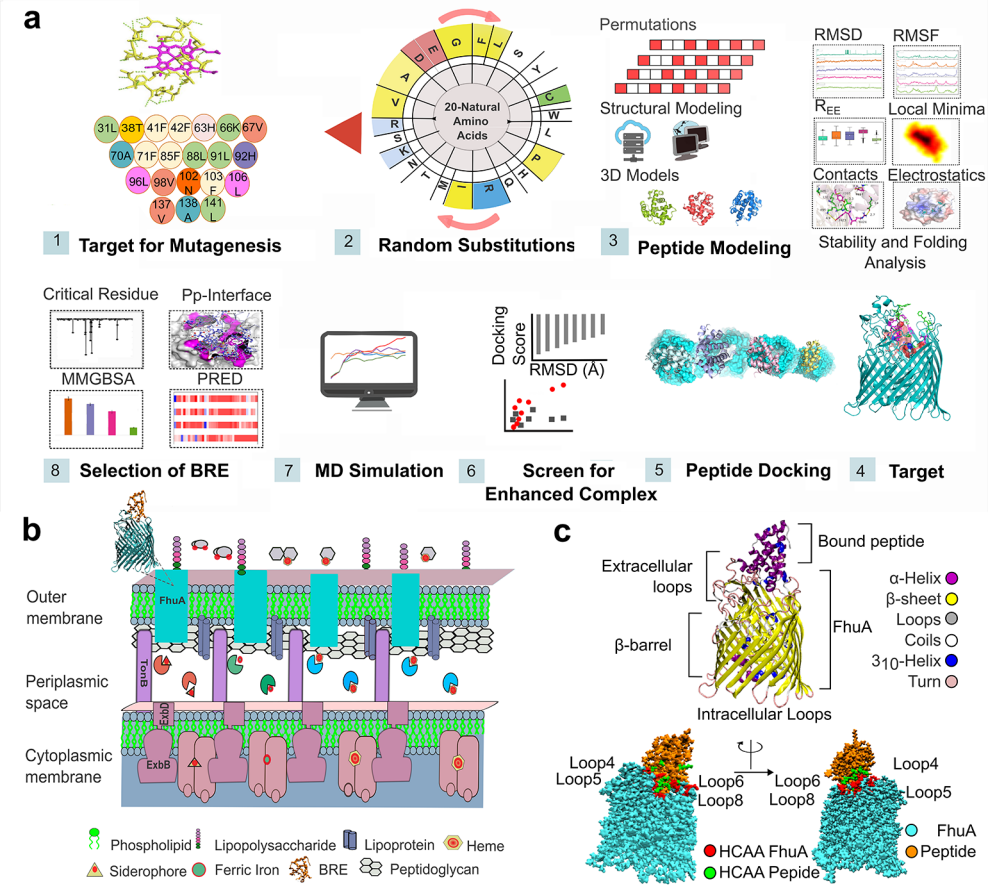

Figure 1. Pipeline for generation of the de novo peptidomimetic recognition element. (a) Overview of peptidomimetics-driven recognition elements design (PepDRED), including design, modeling, and binding activity analysis of AVs. (1) Site defined for targeted mutagenesis. (2) PepDRED obtains permutations for AVs through automated incorporation of natural amino acids. (3) Computational workflow for modeling AVs from 1D to 3D structures. Subpanel on the right elucidates factors considered to evaluate the stability of AVs and the validation of 3D structures. (4) Putative binding pocket of target protein for localized docking analysis of AVs. (5) After localized docking, bound complexes are obtained. (6) Bound complexes are screened via plotting fitness value D2 (docking energy score-G/RMSD-R) against RMSD. (7) Binding affinity of better-docked complexes is analyzed through MD simulation. (8) MD simulation analysis unravels the critical amino acids for target stabilization at the protein-peptide interactions, and MMGBSA shows a strong binding affinity by lead AV440. (b) Binding of peptides as BRE to iron transporter FhuA. (c) Secondary structural composition of FhuA_AV complex (first row) and position of highly contributing amino acids (HCAA) at the FhuA_AV interface (second row).

iaceae strains, such as *Escherichia coli*, which frequently acquire AMR.[19] A crucial component conserved in these GNB pathogens is the outer membrane TonB-dependent transporters family of proteins responsible for iron uptake. Iron uptake is an indispensable pathway for the growth and virulence of bacteria.[20] Protein−protein interactions between bacterial outer membrane receptors and a host iron carrier protein (e.g., hemoglobin) facilitate iron uptake.[21,22] In this context, receptor FhuA is well-defined and plays an integral role in the translocation of iron across the outer membrane.[23,24] Previously, this channel has been successfully explored for introducing antibiotics and inhibitors.[23] FhuA-recognizing elements with a high binding affinity and strong interactions can be designed to identify GNBs.

Herein, we designed and simulated peptidomimetics peptides based on human hemoglobin. We applied an automated approach to generate apo variants (AVs) of wild-type hemoglobin β-subunit (WT). First, we generated a pool of hemoglobin peptidomimetics (AVs) and acquired 3D structures using RoseTTAFold. Next, we mechanistically elucidated the stability of the AVs through molecular dynamics (MD) simulations. Finally, we showcased the AVs' selectivity and binding affinities to FhuA by identifying the interactions and measuring energy networks produced by molecular mechanics generalized Born surface areas (MMGBSA) and per residue energy decomposition analysis (PRED).[25] Combining the hemoglobin-mimicking capability of AVs and strong binding affinity, we demonstrated that AVs can potentially be applied as stable BREs for FhuA (Figure 1).

RESULTS AND DISCUSSION

Design and Selection of the Multiple AVs via PepDRED. To identify FhuA-responsive peptide sequences, we apply a rational design peptidomimetics approach via PepDRED, leveraging hemoglobin's natural interaction with FhuA. Although α and β subunits of hemoglobin are precursors of various peptides, our study specifically utilizes β-hemoglobin as a template, attributed to its distinct ability to produce host defense peptides.[26] As a means to generate AVs, the evolutionary information is scripted in our python code (available as Supporting Information). In our preliminary investigation, which involves examining the influence of

https://doi.org/10.1021/acs.analchem.3c01057
Anal. Chem. 2023, 95, 12264−12272

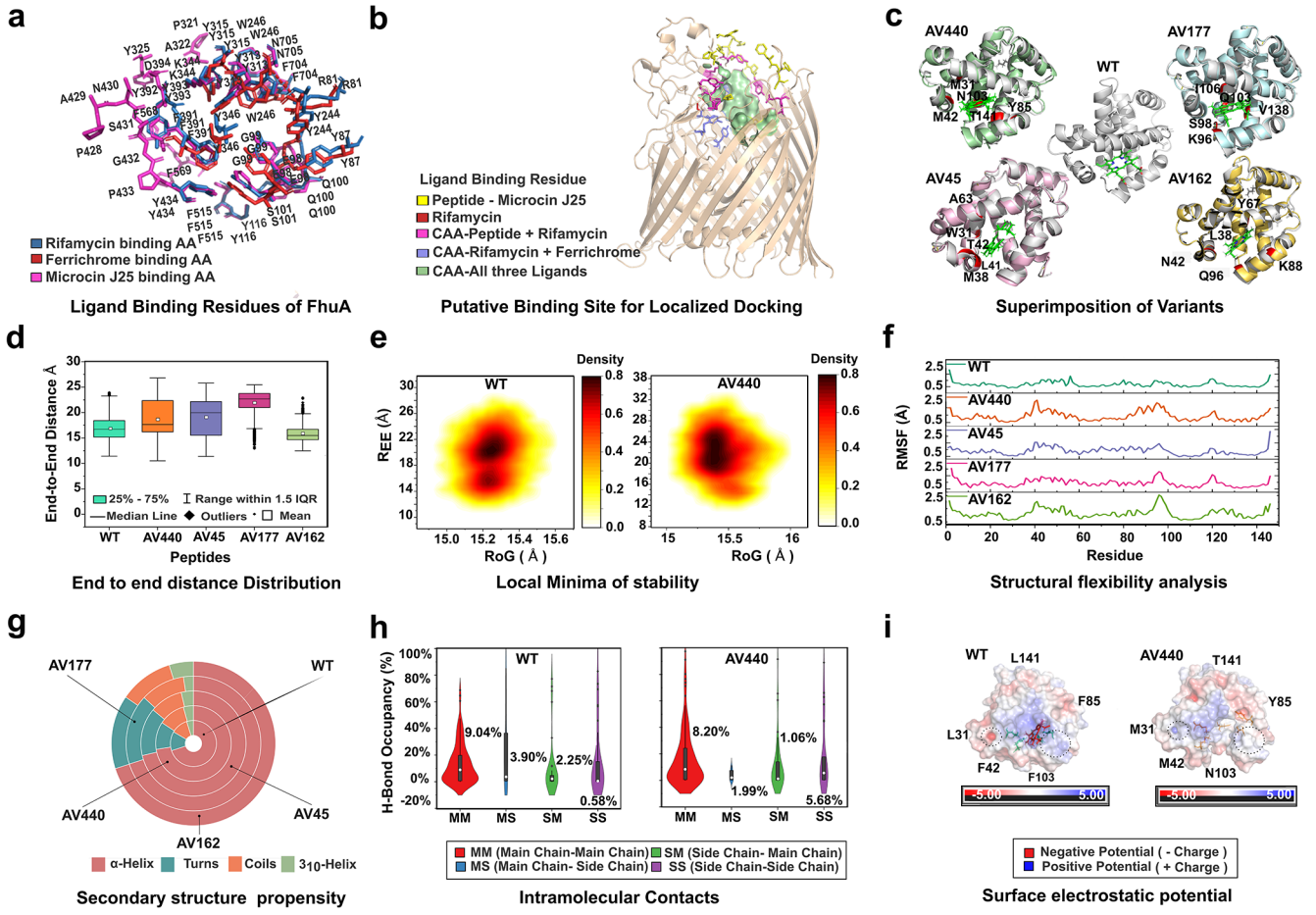

Figure 2. Restraints for localized docking and stability analysis of AVs. (a) FhuA ligand binding residues acquired from the analysis of three FhuA bioactive ligands are applied for AVs localized docking. (b) Ligand binding residues of FhuA, their location, and nature of conservation across three ligands (see also Table S2). (c) Superimposition of equilibrated structures of AVs to WT show complementarity. (d) The end-to-end distance (R_{EE}) analysis throughout the MD simulation shows statistically insignificant changes. However, there are intermittent fluctuations, represented by the outliers and whiskers. (e) Black basins show local minima, which indicate the minimum R_{EE} and RoG values for stable AV structures. (f) RMSF of the WT and AVs. Mutated residues in AVs demonstrate greater flexibility, indicating that increased movement may alter the function of AVs. (g) Secondary structural propensity shows an increase in α-helices in AVs due to mutations. (h) Intramolecular hydrogen bonding shows a decrease in main-chain (MM) interactions, while side-chain (SS) interactions increase in AVs. The median percentage of each kind of interaction is given. (i) Electrostatic surface potential indicates mutated amino acids mainly show positive electrostatic potential tendencies relative to WT.

various mutation counts within our template's defined mutagenesis site, we identify that introducing five mutations markedly enhances the docking scores. This initial finding is instrumental in guiding us to implement five mutations standard for designing our optimized peptide library (Table S1). PepDRED initializes automated site-directed mutagenesis and generates a pool of 500 permutations of WT. Each permutation contains five random amino acid mutations (Table S1). RoseTTAFold models AVs and 3D structures are cross-verified by AlphaFold2, which validates their accuracy (Figure S1).

Binding Analysis and Stability of AVs. Localized docking is performed to determine the specific binding of AVs to FhuA (Figure 2a,b and Table S2), and thus bound FhuA_AV complexes are obtained (Figure 2c). The 3D structures of 500 AVs undergo molecular docking.[27] Our analysis indicates that AVs dock specifically at the FhuA entry channel. Subsequently, we derive a set of bound candidates (FhuA_AV), curated and sorted by their respective docking energy scores (Figure S2). To obtain the best-fit stable complexes, we applied the ratio of the docking energy score to the RMSD to obtain an energy score (D2). Followed by the plotting of D2 against RMSD (R) of bounded FhuA_AVs, we obtain the final four stable and high-scoring complexes in the order of FhuA_AV440 > FhuA_AV45 > FhuA_AV177 > FhuA_AV162 for further analysis. The leading ranked pose for each complex is used as the initial coordinate in the MD simulations.

To determine the effects of mutations on stability, we studied the four AVs from the top four complexes in unbounded form and compared their RMSD values to those of the WT.[28] In comparison with WT that exhibits an average RMSD of 1.2 Å with fluctuations until 9 ns, AVs show a more rapid stabilization, reaching RMSD averages of 1.16−1.7 Å at 2 ns. Notably, AV440s stability is highlighted in individual RMSD profiles, with absence of the WT's intermittent fluctuations, signaling its enhanced stability (see Figure S3 for more details). Since the accurate folding of peptides relies on the compactness of structures, we investigated the radius of gyration RoG (Figure S4). The average radii values lie within a range of 15.1−15.4 Å compared to the average RoG of 15.25 Å

https://doi.org/10.1021/acs.analchem.3c01057
Anal. Chem. 2023, 95, 12264−12272

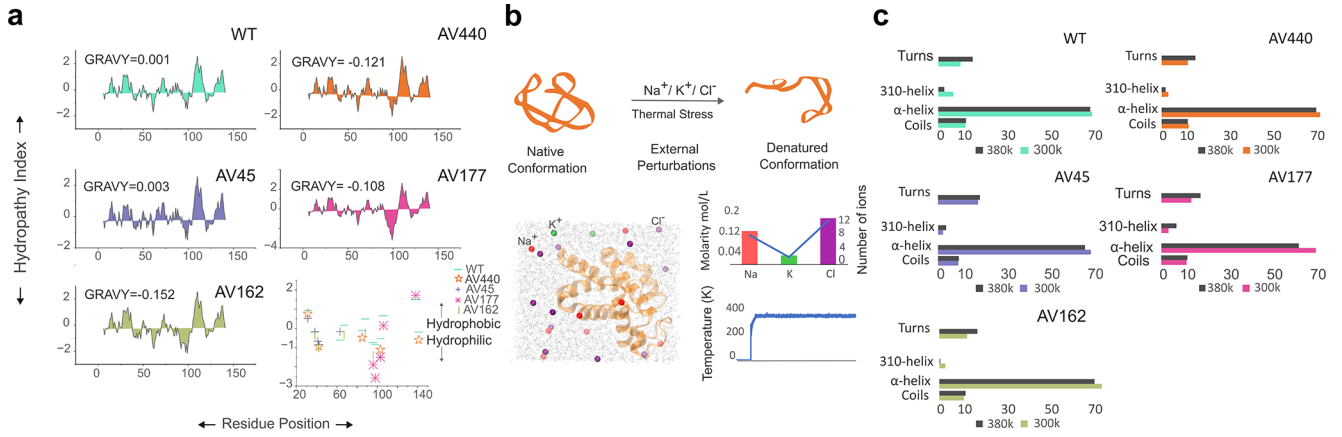

Figure 3. Solubility and adaptive structural flexibility of AVs. (a) The hydropathy index of the top four AVs is compared to that of the WT. Three out of four peptides show a negative GRAVY score, indicating increased solubility. Further, the bottom right panel includes the hydropathy score of introduced mutations, demonstrating the introduction of more hydrophilic amino acids in top AVs. (b) The top row presents a schematic illustrating protein unfolding under ionic and thermal stress, while the bottom row represents the simulation of AV in biological fluid (urine) environment at an increasing temperature. The associated graphs reveal the number of ions introduced and the temperature increase over 50 ns simulation trajectory in urine environment to analyze the folded stability of AVs. (c) Structural flexibility is analyzed by comparing the percentages of secondary structures at 300 K (native conformation) and 380 K (elevated temperature) across all AVs. Our analysis suggests that the AVs maintain their conformation through adaptive structural flexibility under an ionic environment at elevated temperature, with no significant decrease in α-helical structures or significant increase in coils (disordered or misfolded structures).

of WT. The AVs exhibit an insignificant divergence of 0.2−0.5 Å.

On the contrary, the average R_{EE} of AVs fluctuates after mutations. The R_{EE} of WT is approximately 16.96 ± 0.04 Å, while the same values show a cumulative curve in AV440, AV45, and AV177 in order of 18.64 ± 0.03, 19.08 ± 0.04, and 21.91 ± 0.02 Å, respectively, as shown in the Figure 2d. These findings infer an increase of 9.9−29% of the R_{EE} value for WT. On the contrary, R_{EE} shrinks to 15.88 ± 0.03 Å in AV162. Figure 2e depicts the local minima of WT and AV440 as functions of the RoG and R_{EE} distribution. The local minima show two basins of minimal points for stable WT which are 15−17 Å (R_{EE}) and 15.17−15.3 Å (RoG) and 19−23 Å R_{EE} and 15.15−15.35 Å RoG. In contrast, AV440 presents a larger basin from 15−19Å (R_{EE}) to 15.1−15.5 Å (RoG). The larger basin portrays the structural flexibility of AV440 (see Figure S5 for other AVs). Figure 2f presents the root-mean-square fluctuation (RMSF) values for WT and AVs. We observe a stark deviation in the domains corresponding to mutations, more so in AVs than in WT, and it is congruent with the R_{EE} values. AV440 attains higher fluctuations at mutations 4 and 85, and mutations 41 and 42 extend in AV45.AV177 side chain movements are relatively identical to WT, while AV162 shows more fluctuation. All AVs undergo increased flexibility at a patch from residue 90−100 that is predominated by coils in WT. As a consequence of distant and proximal mutations, residues 93, 94, 95 (composed of D, K, L/Q/K—differing due to mutations) display a structural dynamism, transitioning between α-helix and turn structures. As has already been reported, residues like Q, K, and L enhance flexibility owing to their small sizes.[29] This adaptability in structure contributes to maintaining the overall folded stability across all AVs, highlighting the crucial contribution of this patch (Figure S6). Head-on comparison of mutations and sharp fluctuations in RMSF indicate that the flexibility of these domains is enhanced by the mutations (Figure 2c,f). Figure 2g illustrates the calculated secondary structure percentage extracted from MD trajectories for the WT and AVs. Results show that WT has a rich average α-helix structure (69.96%), while the 3_{10}-helix is 4.76%. Turns and coils are ∼11%. In contrast, the AVs reveal a rise in α-helices structures. In AV440, α-helices enhance to 72.5%, representing a 2.5% increase, whereas turns show a relative decrease of 2% compared to that of WT. The average percentage change of coils and 3_{10}-helix structures is insignificant. AV45, AV177, and AV162 show an increase in percentages of α-helix and turns. The percentage of coils decreases across all AVs. We notice that more residues adopt a prominent α-helix structure upon mutations in AVs. Due to the predisposition of α-helices to develop protein−protein interactions, we can assume that it may improve the binding affinity and stabilize FhuA_AVs complexes.[30] Figure 2h shows intramolecular hydrogen bond occupancy in WT and AVs after mutations. According to the findings, the main-chain interactions (MM) declined across the AVs. However, the percentage occupancy of side-chain interactions (SS) enhances. The AV440 shows a median value of 8.20% for MM interactions compared to 9.04% for WT. SS interactions of AV440 present a ∼ 10-fold increase, raising the median to 5.68%. The increment in side-chain hydrogen bonds in AVs may be attributed to the enhanced flexibility of residues due to mutations, evident from the RMSF curve and R_{EE} distance (also see Figure S7). Consequently, although the AVs are compact, the side residues present more surface exposure, and thus, new SS interactions are established. The surface electrostatic potential is calculated to evaluate the effect of random mutations on the overall surface charge. Figure 2f shows the electrostatic potential surfaces of WT and AV440, wherein mutations generate a localized effect and do not alter the overall charge. The surrounding amino acids of mutations may undergo a surface potential change. The electron dense (red) patches may change to electron deficient (blue) regions and vice versa or even turn neutral. Introduced mutations present moderately positive surface potential relative to the WT. Analysis of three other AVs also reveals a positive surface charge distribution leading to electron-deficient stable patches (Figure S8). Besides, the stereochemical quality of AVs is

https://doi.org/10.1021/acs.analchem.3c01057
Anal. Chem. 2023, 95, 12264−12272

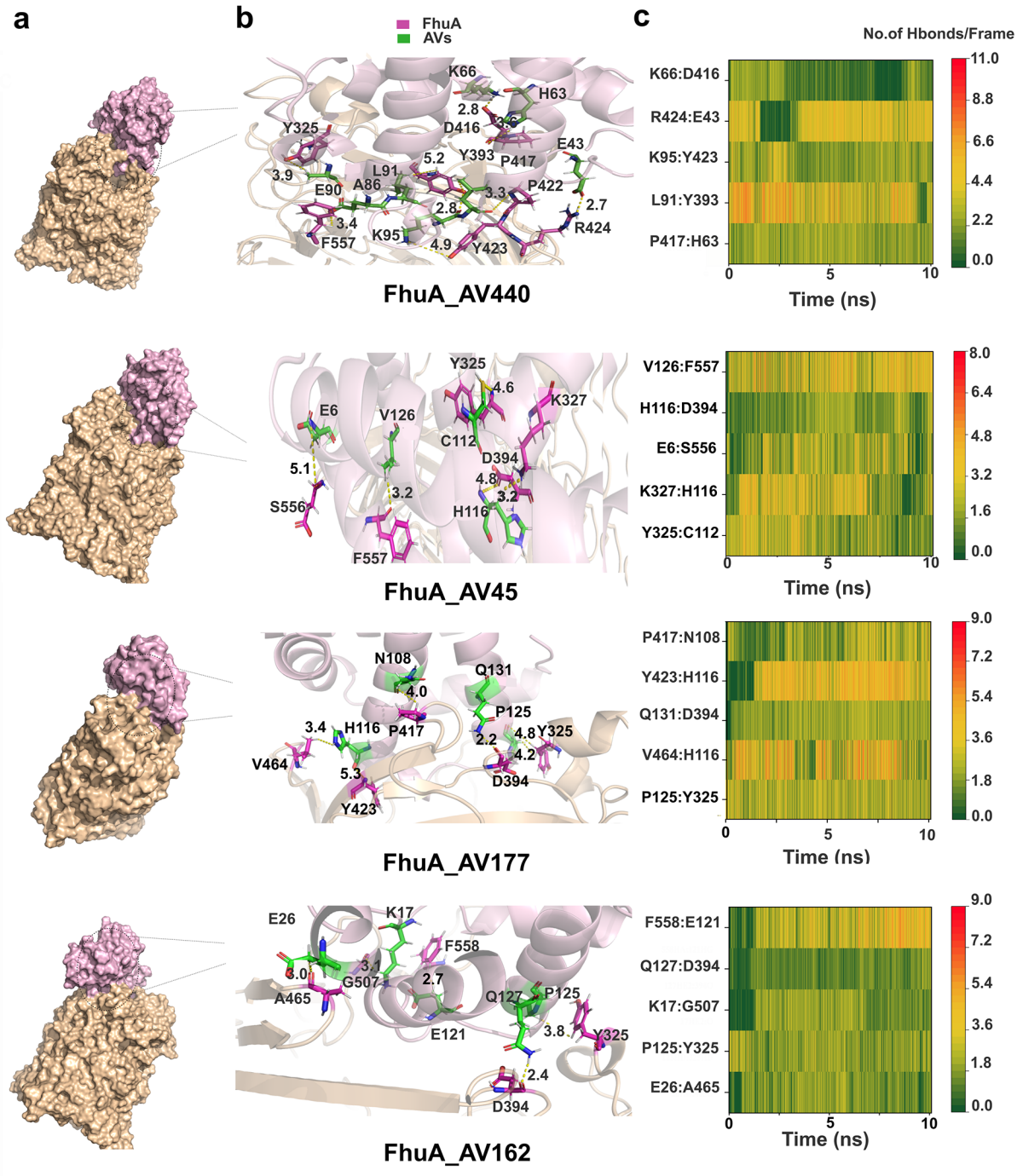

Figure 4. Hydrophilic network interactions enhance the binding affinity of AVs. (a) The best scoring pose of bounded FhuA_AVs complexes selected subsequent to molecular docking for intermolecular network interactions and binding affinity analysis. (b) Detailed atomic interactions of bounded FhuA and AVs are estimated by independent MD simulations. The cutoff distance for hydrogen bonds (H-bonds) is set at 5 Å and DHA angle at 30°. (c) H-bonds occupancy in the complexes over a 10 ns MD trajectory of FhuA_AVs. The heatmaps show the number of H-bonds per frame, and H-bonds with >70% occupancy are presented.

assessed with a Ramachandran plot (RP). Figure S9 shows clear agglomerations in the third quadrant encompassing α-helices. The GRAVY scores show increase hydrophilicity for AV440, AV45, and AV177, and thus validate their enhanced solubility (Figure 3a). Besides, the simulations in urine conditions at elevated temperature provide evidence for folded stability of AVs under stress (Figure 3b,c) through adaptive structural flexibility.

The top four unbounded AVs are essentially identical to that of the WT except for a few minor conformational shifts. Hence, slight differences in R_{EE} and RoG are witnessed. Besides, the results also infer that the residual mutations do not significantly alter the volume significantly. However, the increased flexibility may influence the structure−activity relationship in AVs. Collectively, our results confirm that targeted mutations did not result in misfolding, and AVs are

https://doi.org/10.1021/acs.analchem.3c01057
Anal. Chem. 2023, 95, 12264−12272

Table 1. Energy Components (kcal/mol) of FhuA_AVs' Complexes Calculated via MMGBSA Method[a]

complexes	van der Waals	electrostatics	polar solvation	nonpolar	total binding energy
FhuA−AV440	−82.91 ± 0.36	49.48 ± 0.39	23.5 ± 0.49	−11.07 ± 0.02	−21.00 ± 0.50
FhuA−AV45	−91.83 ± 0.09	142.29 ± 0.6	−56.43 ± 0.8	−11.67 ± 0.05	−17.63 ± 0.3
FhuA−AV177	−94.65 ± 0.12	30.17 ± 1.39	63.21 ± 0.94	−12.1 ± 0.07	−13.37 ± 0.30
FhuA−AV162	−97.92 ± 0.06	64.88 ± 0.19	41.08 ± 0.02	−12.28 ± 0.04	−4.24 ± 0.10

[a]±standard error of the mean (SEM).

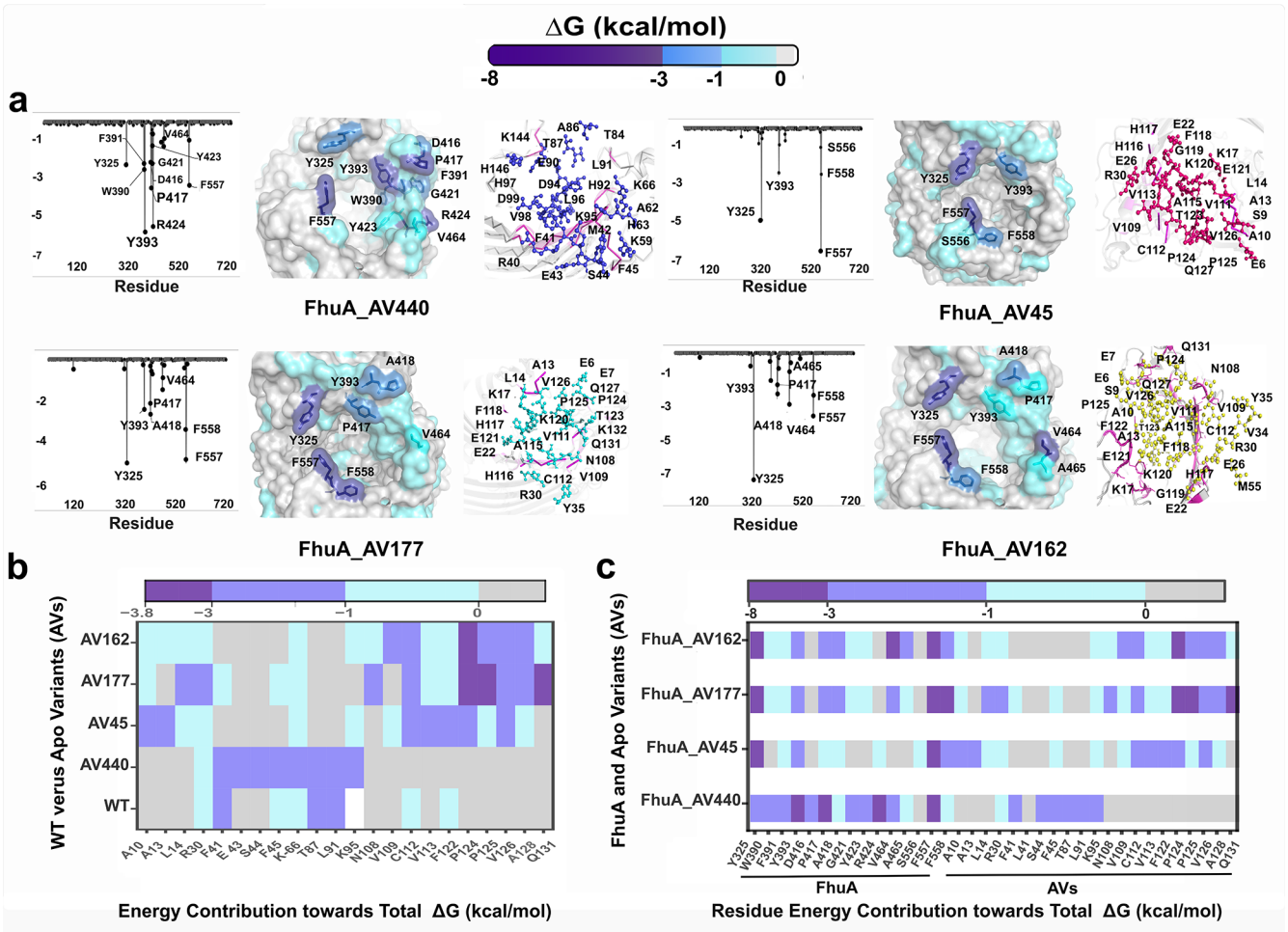

Figure 5. Energetic analysis of FhuA_AVs interfaces. The energy contribution of each residue is calculated through PRED analysis. (a) Left panels present HCAA of FhuA, contributing ≤−1 kcal/mol of stabilizing energy to the total Δ*G* of complexes. Middle panels show a demarcation of FhuA residues at the protein peptide interface (top view). The right panels present a broader picture of AVs' residues as linkers to FhuA at the FhuA_AVs interfaces. (b) HCAA of AVs in bounded form (FhuA_AVs) compared to the interaction energy contribution of the respective residues in WT (FhuA_WT). The results show different sets of critical residues stabilizing the complexes. (c) A comparative analysis of HCAA across four complexes reiterates that mutations lead to changes in networks of interacting residues of AVs and FhuA alike, evident from significant differences in energy contributions among FhuA and AVs.

more stable than WT. Thus, bounded AVs are projected to perform binding affinity analysis.

Protein Peptide Interaction and Binding Efficiency of Bounded AVs via Critical Residues. Figure 4a illustrates the equilibrated poses of bounded FhuA_AVs. Figure 4b explores the hydrogen bonds (H-bonds) in protein−peptide interaction networks across four complexes. In AV440, H-bond interactions occur with FhuA residues D416, E416, Y423, R424, and Y393, as detailed in Figure 4c. AV45 features E6 binding to S556 and V126 creating double H-bonds with D394 and Y325 of FhuA. AV177's Q131 and P125 form weak H-bonds with FhuA's D394 and Y325, respectively. Similarly, in AV162, residues K17, E26, and P125 form weak H-bonds with FhuA's G507, A465, and D394. Our analysis implies that the high binding affinity of AVs with FhuA stems from interaction with multiple secondary structures, such as *β* barrel and gating loops. The salt bridges formed in the four complexes are listed in Table S3, showing wide discrepancies. AV440 has 10 salt bridges relative to hydrogen bonds counts compared to the 3 for AV45 and AV177 and 1 for AV162 with FhuA. From our analysis of binding interactions, we observe that the H-bond interactions of the AVs with the gating loops of FhuA and salt bridges are crucial for stability. PRED results are delineated in Figure 4. MMGBSA (Table 1), analysis, indicates that AV440 exhibits the most favorable binding affinity (Δ*G* of −21 ± 0.5 kcal/mol), notably surpassing those of AV45 (−17.63 ± 0.3

https://doi.org/10.1021/acs.analchem.3c01057
Anal. Chem. 2023, 95, 12264−12272

kcal/mol) and AV177 (−13.37 ± 0.30 kcal/mol). In contrast to these systems, AV162 underperforms and shows a comparatively low binding affinity of −4.24 ± 0.10 kcal/mol. The interaction energies of each substituted amino acid in the four AVs are given in Table S4. According to the calculated ΔG, AV440 shows ∼2.5-fold increased affinity than that reported for Microcin J25 (MJ25) interaction with FhuA (ΔG bind −8.89 ± 1.32 kcal/mol and ΔG_{exp} bind −8.13 kcal/mol), which is a potent type of antimicrobial peptide (AMP) for FhuA.[31] This increase can be due to the bigger size, higher number of amino acids (146-residues), and extensive residual interactions compared to 21-mer Microcin MJ25 peptide.[32] Moreover, the extended interaction between FhuA and AVs can be ascribed to an increased adaptive flexibility (R_{EE}), potentially enhancing the surface accessible area (SASA) and strengthening intermolecular contacts. PRED is investigated to evaluate the impact of mutations on individual amino acids' contributions to the total ΔG (Figure 5).

Notably, the criterion set for highly contributing amino acid (HCAA) is the contribution of $\Delta G \leq -1.0$ kcal/mol of stabilization energy; these are labeled and discussed hereafter. In congruence with ΔG, Figure 5a shows the HCAA of FhuA, which proactively interacts with AVs. Within the FhuA_AV440 complex, AV440 forms strong bonds with 11 FhuA residues (Y325, V464, W390, F391, Y393, D416, P417, G421, Y423, R424, F557). FhuA's interaction with AV45 and AV177 complexes, however, is limited to only 5 (Y325, Y393, S556, F557, F558) and 7 (Y325, Y393, P417, A418, V464, F557, F558) HCAA, respectively (Figure 5a). Significantly, three residues, Y325, Y393, and F557—on FhuA are consistently involved in the binding of all four AVs, indicating their crucial role in complex stabilization. Particularly, residues Y325 and F557, positioned on loops 4 and 8 (known as FhuA's gating loops), show the highest contributions in all four AVs, ranging from ≥−7.5 to ≤−4.7 and ≥−5.63 to ≤−3.7 kcal/mol, respectively.[33] Besides, V464 (loop 6), F558 (loop 8), and A418 (loop 5) moderately contribute to total ΔG across all bounded AVs (Figure 5a). Although the stabilizing residues of FhuA interact with AV162 alongside five other residues (Y325, Y393, P417, A418, V464, A465, F557, and F558), yet the cumulative binding free energy was comparatively low. In Figure 5b, the PRED analysis reveals a greater contribution of residues toward total ΔG in AVs compared to WT. HCAA in AV440 displays interaction energies ranging from −2.41 to −1.11 kcal/mol, while those in AV45 range from −2.66 to −1.08 kcal/mol. Likewise, significant contributions to complex stabilization with FhuA are made by the HCCA of AV177 and AV162 (Figure 5b,c). These high contributions to the stabilization energies could be ascribed to the modifications in biophysical properties driven by the PepDRED-induced mutations.

Stable AV440 Manifests Potential as a Strong BRE for FhuA. AV440 shows remarkable stability and the highest binding affinity toward FhuA out of a library of 500 AVs. In AV440, random mutations lead to the inclusion of two sulfhydryl groups: namely, F42 mutated to M42 and L31 mutated to M31. Due to these groups, methionine may establish intermolecular contacts with aromatic residues in its vicinity compared to WT (Figure 4b,c). Residues including F41, E43, S44, and F45 show significant improvement in $\Delta G \leq -1$ kcal/mol. The second-best variant AV45 has a ΔG of −17.63 kcal/mol (Table 1) with a decrease of −3 kcal/mol. Although AV45 shows good binding affinity, the contribution of mutations toward ΔG is insignificant. Four of the five mutations are neutral, while L31 in place of W31 shows a slight increase in the binding affinity. However, the flanking residues up to the second neighbors of mutations play a critical role in binding to FhuA, as shown in Figure 4b. Likewise, in AV177, the substitution of A138 by V138-hydrophobic amino acid brings neighboring amino acids to the exposed surface area. As a result, amino acids such as P124, P125, A128, and Q131 show remarkable improvement in ΔG contribution. On the other hand, AV162 performs poorly in binding affinity, having a total ΔG of −4 kcal/mol. The mutations of T38, F42, and V67 to L38, N42, and Y67 do not contribute to the total ΔG, as all of these turn out to be neutral. The substitution of L88 to K88 results in the loss of binding and does not result in a positive contribution either, as the binding energy drops from −0.84 to −0.42 kcal/mol, indicating a destabilizing effect. Our results show that mutations in AV162 lead to the loss of major intermolecular energy contacts. To assess specificity and mitigate potential off-target binding or peptide neutralization, we have also analyzed the interaction of AV440 with different classes of target proteins present in *E. coli* (Figure S10. see Supporting Information for details). AV440s binding affinity for FhuA significantly outperformed its interactions with other potential targets.

The overall analysis of binding energy networks between FhuA and AVs indicates that substituting small amino acids and sulfhydryl groups as methionine (M) exposes the buried regions in their vicinity and alters the binding affinity for FhuA. This is further affirmed by the increased hydrophilicity of AVs. To that end, including M in the N-terminal region of AV440 enhances the binding affinity of neighboring residues significantly. Besides, the exposure of a new set of amino acids results in surface dynamics expansion and an increased quantity of H-bonds and salt bridges. The abundance of these interactions is observed in FhuA_AV440. Additionally, AV440 shows remarkable RMSD, RoG, R_{EE}, hydrophilicity as well as adaptive flexibility and preferential binding for FhuA. Hence, AV440 provides a stable and strongly binding α-helix rich BRE for FhuA biosensing.

CONCLUSIONS

Although bacterial sensors are effective diagnostic tools, the limitations of BREs restrict their application to real samples. Peptides offer a plausible alternative to overcome inherent issues of the stability and affinity of BREs. We devised a new method, namely, PepDRED, to generate peptidomimetics of natural peptides and to identify higher binding BREs for iron transporter FhuA. We applied the PepDRED pipeline to derive a strong binding and stable BRE_AV440 via hydrophilic interactions.

Moreover, the inclusion of methionine mutations in the peptide sequence exemplifies a potent strategy for future designs, primarily due to its capacity to enhance the physicochemical properties of the peptides. PepDRED can modulate the AV440 scaffold by preserving the HCAA while modifying the rest of the amino acids for the optimization and evolution of future BRE designs. In addition, once bound with a transducer, our stable and firmly binding BRE_AV440 can be integrated into a bacterial diagnostic biosensor.

https://doi.org/10.1021/acs.analchem.3c01057
Anal. Chem. 2023, 95, 12264−12272

EXPERIMENTAL SECTION

Peptidomimetics Driven Recognition Element Design. In PepDRED, peptide evolution begins with identifying the heme-binding pocket in WT. For site-directed mutation, the residues within 5 Å of the cofactor are selected for designing stable and strong affinity AVs. Twenty-one residues in WT constitute heme binding pocket, namely, L31, T38, F41, F42, H63, K66, V67, A70, F71, F85, L88, L91, H92, L96, V98, N102, F103, L106, V137, A138, and L141. For the sake of automation, a Python script is developed. The script keeps the heme binding pocket "variable", while the rest of the scaffold β-subunit is "invariable", allowing naturally occurring amino acids to mutate the "variable" region randomly. The number of amino acid mutations per sequence is decided sequentially and evaluated via docking energy score (see Figure S1). The mutations thus introduced are not redundant, and each sequence differs from another. After that, a pool of sequences of AVs is generated for modeling. Next, we apply RoseTTAFold to generate the 3D structure of AVs for high-binding-affinity studies (for detailed methodology, see Supporting Information).

ASSOCIATED CONTENT

Supporting Information

The Supporting Information is available free of charge at https://pubs.acs.org/doi/10.1021/acs.analchem.3c01057.

PepDRED python code, experimental details, initial screening via Docking score, cross-validation of AVs. Additional biophysical properties' analysis of AVs (RoG distribution graph, electrostatic surface potential, conformational drifts, RP) result and discussion for specificity analysis, table for docking restraints, introduced mutations and energy contributions of mutations and SASA are shown in Supporting Information (PDF)

AUTHOR INFORMATION

Corresponding Authors

Lai Jiang − *Department of Anesthesiology and Surgical Intensive Care Unit, Xinhua Hospital, School of Medicine and School of Biomedical Engineering and State Key Laboratory of Oncogenes and Related Genes, Institute for Personalized Medicine, Shanghai Jiao Tong University, Shanghai 200230, China*; Email: jianglai@xinhuamed.com.cn

Xianting Ding − *Department of Anesthesiology and Surgical Intensive Care Unit, Xinhua Hospital, School of Medicine and School of Biomedical Engineering and State Key Laboratory of Oncogenes and Related Genes, Institute for Personalized Medicine, Shanghai Jiao Tong University, Shanghai 200230, China*; orcid.org/0000-0002-1549-3499; Email: dingxianting@sjtu.edu.cn

Authors

Mehmoona Azmat − *Department of Anesthesiology and Surgical Intensive Care Unit, Xinhua Hospital, School of Medicine and School of Biomedical Engineering and State Key Laboratory of Oncogenes and Related Genes, Institute for Personalized Medicine, Shanghai Jiao Tong University, Shanghai 200230, China*

Behafarid Ghalandari − *State Key Laboratory of Oncogenes and Related Genes, Institute for Personalized Medicine, Shanghai Jiao Tong University, Shanghai 200230, China*

Jessica Jessica − *State Key Laboratory of Oncogenes and Related Genes, Institute for Personalized Medicine, Shanghai Jiao Tong University, Shanghai 200230, China*

Yuechen Xu − *State Key Laboratory of Oncogenes and Related Genes, Institute for Personalized Medicine, Shanghai Jiao Tong University, Shanghai 200230, China*

Xinle Li − *State Key Laboratory of Oncogenes and Related Genes, Institute for Personalized Medicine, Shanghai Jiao Tong University, Shanghai 200230, China*

Wenqiong Su − *State Key Laboratory of Oncogenes and Related Genes, Institute for Personalized Medicine, Shanghai Jiao Tong University, Shanghai 200230, China*

Zhang Qiang − *State Key Laboratory of Oncogenes and Related Genes, Institute for Personalized Medicine, Shanghai Jiao Tong University, Shanghai 200230, China*

Shuxin Deng − *State Key Laboratory of Oncogenes and Related Genes, Institute for Personalized Medicine, Shanghai Jiao Tong University, Shanghai 200230, China*

Tabina Azmat − *Department of Cyber Security, AIR University, Islamabad 44000, Pakistan*

Complete contact information is available at: https://pubs.acs.org/10.1021/acs.analchem.3c01057

Notes

The authors declare no competing financial interest.

ACKNOWLEDGMENTS

We gratefully thank the financial support from NSFC Projects (T2122002, 22077079, 81871448), Ministry of Science and Technology of China Projects (2022YFC2601700, 2022YFF0710202), Shanghai Municipal Science and Technology Project (22Z510202478), Shanghai Municipal Education Commission Project (21SG10), Shanghai Jiao Tong University Projects (YG2021ZD19, Agri-X20200101, 2020 SJTU-HUJI), Shanghai Municipal Health Commission Project (2019CXJQ03). Thanks to AEMD SJTU, Shanghai Jiao Tong University Laboratory Animal Center, for the technical support.

REFERENCES

(1) Jones, K. E.; Patel, N. G.; Levy, M. A.; Storeygard, A.; Balk, D.; Gittleman, J. L.; Daszak, P. *Nature* **2008**, *451* (7181), 990−993.
(2) Goff, D. A.; Mendelson, M. *Lancet Infect. Dis.* **2014**, *14* (12), 1168−1169.
(3) Ventola, C. L. *PT* **2015**, *40*, 277.
(4) Giardi, M. T.; Piletska, E. V. *Biotechnological Applications of Photosynthetic Proteins: Biochips, Biosensors and Biodevices*; Springer Science & Business Media, 2006.
(5) Kulagina, N. V.; Lassman, M. E.; Ligler, F. S.; Taitt, C. R. *Anal. Chem.* **2005**, *77* (19), 6504−6508.
(6) Morales, M. A.; Halpern, J. M. *Bioconjugate Chem.* **2018**, *29* (10), 3231−3239.
(7) Chen, J.; Jiang, Z.; Ackerman, J. D.; Yazdani, M.; Hou, S.; Nugen, S. R.; Rotello, V. M. *Analyst* **2015**, *140* (15), 4991−4996.
(8) Majdinasab, M.; Hayat, A.; Marty, J. L. *TrAC, Trends Anal. Chem.* **2018**, *107*, 60−77.
(9) Huang, C.-C.; Chen, C.-T.; Shiang, Y.-C.; Lin, Z.-H.; Chang, H.-T. *Anal. Chem.* **2009**, *81* (3), 875−882.
(10) Hillman, Y.; Gershberg, J.; Lustiger, D.; Even, D.; Braverman, D.; Dror, Y.; Ashur, I.; Vernick, S.; Sal-Man, N.; Wine, Y. *Anal. Chem.* **2021**, *93* (2), 928−935.
(11) Cheng, D.; Yu, M.; Fu, F.; Han, W.; Li, G.; Xie, J.; Song, Y.; Swihart, M. T.; Song, E. *Anal. Chem.* **2016**, *88* (1), 820−825.

(12) Ahmed, A.; Rushworth, J. V.; Hirst, N. A.; Millner, P. A. *Clin. Microbiol. Rev.* **2014**, *27* (3), 631−646.
(13) Tombelli, S.; Minunni, M.; Mascini, M. *Biomol. Eng.* **2007**, *24*, 191−200.
(14) Wang, J.; McIvor, M. J.; Elliott, C. T.; Karoonuthaisiri, N.; Segatori, L.; Biswal, S. L. *Anal. Chem.* **2014**, *86* (3), 1671−1678.
(15) Fabrizio, A.; Grisafi, A.; Meyer, B.; Ceriotti, M.; Corminboeuf, C. *Chem. Sci.* **2019**, *10* (41), 9424−9432.
(16) Chou, S.; Wang, J.; Shang, L.; Akhtar, M. U.; Wang, Z.; Shi, B.; Feng, X.; Shan, A. *Biomater. Sci.* **2019**, *7* (6), 2394−2409.
(17) Jumper, J.; Hassabis, D. *Nat. Methods* **2022**, *19* (1), 11−12.
(18) Baek, M.; DiMaio, F.; Anishchenko, I.; Dauparas, J.; Ovchinnikov, S.; Lee, G. R.; Wang, J.; Cong, Q.; Kinch, L. N.; Schaeffer, R. D.; et al. *Science* **2021**, *373* (6557), 871−876.
(19) Exner, M.; Bhattacharya, S.; Christiansen, B.; Gebel, J.; Goroncy-Bermes, P.; Hartemann, P.; Heeg, P.; Ilschner, C.; Kramer, A.; Larson, E.; et al. *GMS Hyg. Infect. Control* **2017**, *12*, Doc05.
(20) Tang, F.; Saier, M. H. *Microb. Pathog.* **2014**, *71*−*72*, 41−55.
(21) Mosbahi, K.; Wojnowska, M.; Albalat, A.; Walker, D. *Proc. Natl. Acad. Sci. U.S.A.* **2018**, *115* (26), 6840−6845.
(22) Braun, V.; Braun, M. *FEBS Lett.* **2002**, *529* (1), 78−85.
(23) Klebba, P. E.; Newton, S. M. C.; Six, D. A.; Kumar, A.; Yang, T.; Nairn, B. L.; Munger, C.; Chakravorty, S. *Chem. Rev.* **2021**, *121* (9), 5193−5239.
(24) Koebnik, R.; Locher, K. P.; Van Gelder, P. *Mol. Microbiol.* **2000**, *37* (2), 239−253.
(25) Rastelli, G.; Del Rio, A.; Degliesposti, G.; Sgobba, M. *J. Comput. Chem.* **2010**, *31* (4), 797−810.
(26) Sheshadri, P.; Abraham, J. *Immunopharmacol. Immunotoxicol.* **2012**, *34* (6), 896−900.
(27) Yan, Y.; Tao, H.; He, J.; Huang, S.-Y. *Nat. Protoc.* **2020**, *15* (5), 1829−1852.
(28) Dixit, S. B.; Ponomarev, S. Y.; Beveridge, D. L. *J. Chem. Inf. Model.* **2006**, *46* (3), 1084−1093.
(29) Zhao, S.; Goodsell, D. S.; Olson, A. J. *Proteins* **2001**, *43* (3), 271−279.
(30) Abrusán, G.; Marsh, J. A. *PLoS Comput. Biol.* **2016**, *12* (12), No. e1005242.
(31) Lai, P. K.; Kaznessis, Y. N. *J. Chem. Theory Comput.* **2017**, *13* (7), 3413−3423.
(32) Li, Z.; Chinnasamy, S.; Zhang, Y.; Wei, D. Q. *J. Biomol. Struct. Dyn.* **2021**, *39* (7), 2585−2594.
(33) Endriß, F.; Braun, M.; Killmann, H.; Braun, V. *J. Bacteriol.* **2003**, *185*, 4683−4692.

https://doi.org/10.1021/acs.analchem.3c01057
Anal. Chem. 2023, 95, 12264−12272